ACS APPLIED MATERIALS & INTERFACES

www.acsami.org

Research Article

Two-Dimensional Metal Halide Perovskites Created by Binary Conjugated Organic Cations for High-Performance Perovskite Photovoltaics

Lening Shen, Haodong Wu, Zikun Cao, Xiyao Zhang, Lei Liu, Hussain Sawwan, Tao Zhu, Jie Zheng, He Wang,* and Xiong Gong*

Cite This: *ACS Appl. Mater. Interfaces* 2024, 16, 19318−19329

Read Online

ACCESS | Metrics & More | Article Recommendations | Supporting Information

ABSTRACT: Studies indicated that two-dimensional (2D) metal halide perovskites (MHPs) embodied with three-dimensional (3D) MHPs were a facile way to realize efficient and stable perovskite solar cells (PSCs) and perovskite photodetectors (PPDs). Here, high-performance PSCs and PPDs, which are based on 2D/3D MHPs bilayer thin films, where the 2D MHPs are created by binary conjugated organic cations, are reported. Systemically studies reveal that the above novel 2D/3D MHPs bilayer thin films possess an enlarged crystal size, balanced charge transport, reduced charge carrier recombination, smaller charge-transfer resistance, and accelerated charge-extraction process compared to the 2D/3D MHPs bilayer thin films, where the 2D MHPs are created by a single conjugated organic cation. As a result, the PSCs based on the above novel 2D/3D MHPs bilayer thin film exhibit a power conversion efficiency of 22.76%. Moreover, unencapsulated PSCs possess dramatically enhanced stability compared with those based on the 2D/3D MHPs bilayer thin films, where the 2D MHPs are created by a single conjugated organic cation. In addition, the PPDs based on the above novel 2D/3D MHPs bilayer thin film exhibit a projected detectivity of 10^{16} cm $Hz^{1/2}$/W and a linear dynamic range of 108 dB at room temperature. Our studies indicate that the development of binary conjugated organic cation-based 2D MHPs incorporated with 3D MHPs is a simple method to realize high-performance PSCs and PPDs.

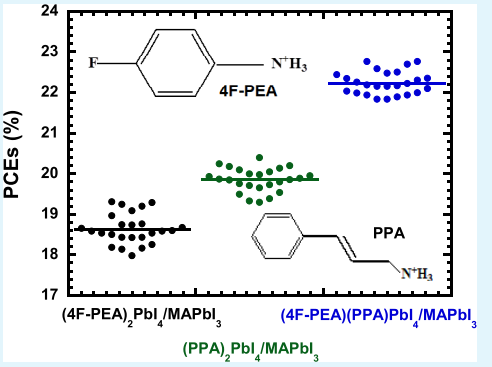

KEYWORDS: *2D perovskites, binary conjugated organic cations, perovskite solar cells, perovskite photodetectors, efficiency, stability, detectivity*

1. INTRODUCTION

Studies demonstrated that metal halide perovskites (MHPs) were one kind of novel promising photovoltaic materials to realize cost-effective perovskite solar cells (PSCs) and perovskite photodetectors (PPDs).[1−8] Over 26% power convention efficiency (PCE) from PSCs and ∼10^{15} cm $Hz^{1/2}$/W (Jones) projected detectivity (D^*) from PPDs have been reported from meso-superstructured devices by three-dimensional (3D) MHPs.[8−11] However, 3D MHPs are unstable in an ambient atmosphere; hence, the PSCs and PPDs based on the 3D MHPs are unstable in the air with moisture.[12−16] To address these issues, 2D MHPs, where the small-sized organic hydrophilic cations were substituted by large-sized organic hydrophobic cations, have been developed.[17−19] Compared to 3D MHPs, 2D MHPs are insensitive to moisture and oxygen.[14,17−20] Further studies demonstrated that the 3D MHPs incorporated with 2D MHPs were an uncomplicated way to realize high-performance PPVs.[8,17−21] The 2D MHPs based on different insulating organic cations have been reported.[5,17−23] However, these 2D MHPs possess poor charge transport, thereby suppressing the photocurrent enhancement, which restricts the device's performance.[24−34] To address these problems, conjugated organic cations were used to generate 2D MHPs.[23,35−40] For example, we reported high-performance PSCs and PPDs, which were fabricated by 3D MHPs incorporated with the 2D MHPs, where the 2D MHPs were created by conjugated organic cations.[8,20,35]

The 2D MHPs based on binary insulating organic cations were developed for approaching stable and efficient PSCs.[24,41,42] In 2020, Shao and co-workers reported enhanced PCEs and stability from the PSCs incorporated with 2D MHPs, which were based on the two bulky insulating organic cations.[41] An efficient PSCs incorporated with the 2D MHPs, which were based on the mixed insulating organic cations was also reported by Zhou et al.[26] All of these studies indicated that

Received: January 5, 2024
Revised: March 22, 2024
Accepted: March 26, 2024
Published: April 5, 2024

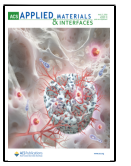

https://doi.org/10.1021/acsami.4c00288
ACS Appl. Mater. Interfaces 2024, 16, 19318−19329

boosted PCEs could be realized from the PSCs incorporated with binary insulating organic cation-based 2D MHPs. So far, however, the development of binary conjugated organic cation-based 2D MHPs for approaching high-performance PSCs and PPDs has been rarely reported.

In this study, we reported high-performance PSCs and PPDs, which are fabricated by 2D/3D MHPs bilayer thin films, where the 2D MHPs are created by binary conjugated organic cations. Compared to the $(4F\text{-}PEA)_2PbI_4/MAPbI_3$ and $(PPA)_2PbI_4/MAPbI_3$ bilayer thin film, enlarged crystal sizes, a tendency of balanced charge transport, reduced charge carrier recombination and charge-transfer resistance, and accelerated charge-extraction time are observed from the (4F-PEA)(PPA)-$PbI_4/MAPbI_3$ bilayer thin film, where 4F-PEA is 4-fluorophenethylamine, and PPA is 3-phenyl-2-propen-1-amine (Scheme 1). As a result, the PSCs fabricated by (4F-PEA)(PPA)$PbI_4/MAPbI_3$ bilayer thin films exhibit a PCE of 22.76%. Moreover, unencapsulated PSCs based on the (4F-PEA)(PPA)$PbI_4/MAPbI_3$ bilayer thin films degrade 50% after 2900 h of operation in the air with a 25% relative humidity at room temperature (RT). In addition, the PPDs fabricated by the (4F-PEA)(PPA)$PbI_4/MAPbI_3$ bilayer thin film possess a D^* of 1×10^{16} Jones and a linear dynamic range of 108 dB at RT.

Scheme 1. Molecular Structures of 4-Fluorophenylammonium (4F-PEA) and 3-Phenyl-2-propen-1-amine (PPA)

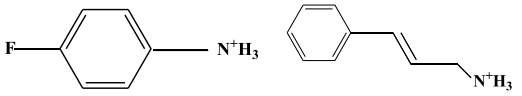

4F-PEA PPA

2. RESULTS AND DISCUSSION

Scheme 2 displays the top-view scanning electron microscope (SEM) images and crystal size distributions of the $(4F\text{-}PEA)_2PbI_4/MAPbI_3$, $(PPA)_2PbI_4/MAPbI_3$, and (4F-PEA)-(PPA)$PbI_4/MAPbI_3$ bilayer thin films. Compared to 3D $MAPbI_3$,[5,43] both $(4F\text{-}PEA)_2PbI_4/MAPbI_3$ and $(PPA)_2PbI_4/MAPbI_3$ bilayer thin film possess a rough surface and large crystals, with bright grain spots, which indicate that both 2D $(4F\text{-}PEA)_2PbI_4$ and $(PPA)_2PbI_4$ thin film are indeed formed on the top of 3D $MAPbI_3$ thin film, creating the $(4F\text{-}PEA)_2PbI_4/MAPbI_3$ and $(PPA)_2PbI_4/MAPbI_3$ bilayer thin films.[5,35] Similarly, the (4F-PEA)(PPA)$PbI_4/MAPbI_3$ bilayer thin film has large crystals, which demonstrates that the 2D (4F-PEA)(PPA)PbI_4 thin film is over the 3D $MAPbI_3$ thin film. However, these three 2D/3D MHPs bilayer thin films possess different crystal sizes (Scheme 2d). The average crystal sizes for the $(4F\text{-}PEA)_2PbI_4/MAPbI_3$, $(PPA)_2PbI_4/MAPbI_3$, and (4F-PEA)(PPA)$PbI_4/MAPbI_3$ bilayer thin films are ~380, ~300, and 460 nm, respectively. Such large crystal sizes imply that these bilayer thin films probably possess high charge carrier mobilities and boosted charge transport.

According to the space-charge-limited current (SCLC) method based on the Mott−Gurney model,[44,45] charge carrier mobilities of the 2D/3D MHPs bilayer thin films are investigated. The current versus voltage (I−V) characteristics of the hole-only diodes and the electron-only diodes (Scheme S1 in SI 1), measured in the dark, are shown in Figure 1. The charge carrier mobility (μ) is described as $J = \frac{9\varepsilon\varepsilon_0\mu V^2}{8L^3}$,[44,45] where J is the current density, V is the external bias, L is the thickness of the active layer, ε_0 is the vacuum permittivity (8.55 $\times 10^{-12}$ F m^{-1}), and ε is the relative dielectric constant for the active layer (Figure S1). The hole mobilities for the $(4F\text{-}PEA)_2PbI_4/MAPbI_3$, $(PPA)_2PbI_4/MAPbI_3$, and (4F-PEA)-(PPA)$PbI_4/MAPbI_3$ bilayer thin films are evaluated to be ~1.50 $\times 10^{-3}$, ~5.40 $\times 10^{-3}$ and ~7.40 $\times 10^{-3}$ cm^2 V^{-1} s^{-1}, respectively. The electron mobilities for the $(4F\text{-}PEA)_2PbI_4/$

Scheme 2. Top-View SEM Images of (a) $(4F\text{-}PEA)_2PbI_4/MAPbI_3$, (b) $(PPA)_2PbI_4/MAPbI_3$, and (c) (4F-PEA)(PPA)$PbI_4/MAPbI_3$ Bilayer Thin Films, and (d) Crystal Size Distribution of the $(4F\text{-}PEA)_2PbI_4/MAPbI_3$, $(PPA)_2PbI_4/MAPbI_3$, and (4F-PEA)(PPA)$PbI_4/MAPbI_3$ Bilayer Thin Films

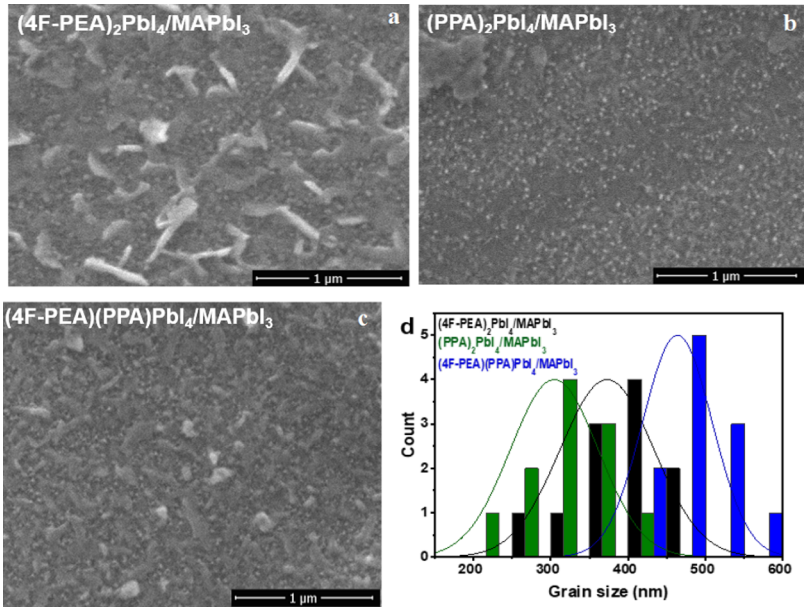

https://doi.org/10.1021/acsami.4c00288
ACS Appl. Mater. Interfaces 2024, 16, 19318−19329

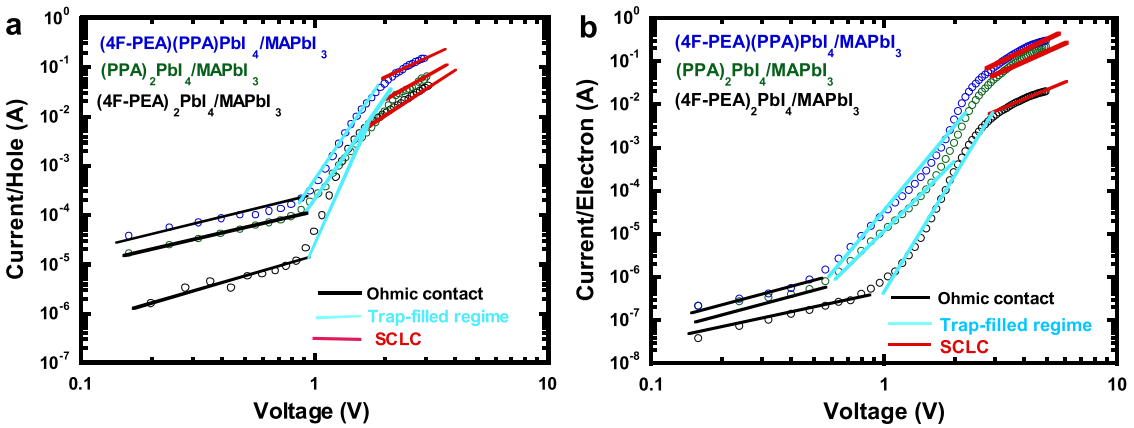

Figure 1. *I*−*V* characteristics of the (a) hole-only and (b) electron-only diodes based on the $(4F\text{-}PEA)_2PbI_4/MAPbI_3$, $(PPA)_2PbI_4/MAPbI_3$, and $(4F\text{-}PEA)(PPA)PbI_4/MAPbI_3$ bilayer thin films.

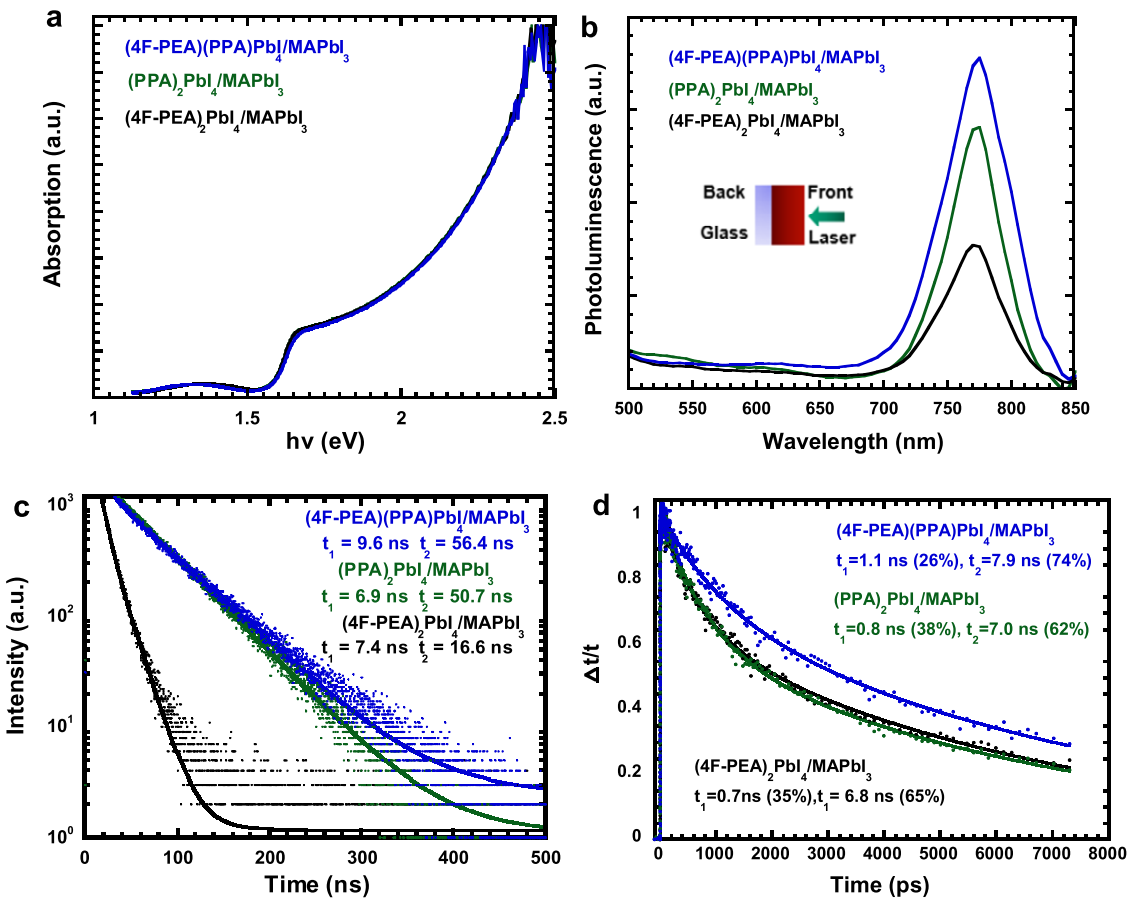

Figure 2. (a) Tauc plot from absorption, (b) photoluminescence (PL) spectra under the light illumination from the front side, (c) time-resolved PL (TR-PL) and (d) transient absorption (TA) kinetics of the $(4F\text{-}PEA)_2PbI_4/MAPbI_3$, $(PPA)_2PbI_4/MAPbI_3$, and $(4F\text{-}PEA)(PPA)PbI_4/MAPbI_3$ bilayer thin films.

$MAPbI_3$, $(PPA)_2PbI_4/MAPbI_3$, and $(4F\text{-}PEA)(PPA)PbI_4/MAPbI_3$ bilayer thin films are evaluated to be $\sim 3.30 \times 10^{-4}$, $\sim 2.90 \times 10^{-3}$, and $\sim 5.10 \times 10^{-3}$ $cm^2\ V^{-1}\ s^{-1}$, respectively. Thus, compared to the $(4F\text{-}PEA)_2PbI_4/MAPbI_3$ and $(PPA)_2PbI_4/MAPbI_3$ bilayer thin films, both hole and electron mobility of the $(4F\text{-}PEA)(PPA)PbI_4/MAPbI_3$ bilayer thin film are enhanced, thereby resulting in an enhanced charge transport.

The $(4F\text{-}PEA)_2PbI_4/MAPbI_3$ bilayer thin film possesses the lowest charge carrier mobility, and the $(4F\text{-}PEA)(PPA)PbI_4/MAPbI_3$ bilayer thin film possesses the highest one, whereas the $(PPA)_2PbI_4/MAPbI_3$ bilayer thin film has higher charge carrier mobility than that of the $(4F\text{-}PEA)_2PbI_4/MAPbI_3$ bilayer thin film. Such a higher charge carrier mobility is probably ascribed to the more delocalized electron density within PPA than that within 4F-PEA. Such a high delocalized electron density could boost the electronic conductivity of the $(PPA)_2PbI_4/MAPbI_3$ bilayer thin film, resulting in enhanced charge carrier mobility. On the other hand, 4F-PEA is more hydrophobic than PPA. Thus, the interface between (4F-

https://doi.org/10.1021/acsami.4c00288
ACS Appl. Mater. Interfaces 2024, 16, 19318−19329

$PEA)_2PbI_4$ and $MAPbI_3$ is different from that between $(PPA)_2PbI_4$ and $MAPbI_3$, which could also affect charge carrier mobility of the resultant 2D/3D MHPs bilayer. An enhanced electronic conductivity induced by PPA and a superior interface originated by 4F-PEA could boost the charge carrier mobility of the (4F-PEA)(PPA)PbI_4/$MAPbI_3$ bilayer thin film.

Moreover, Scheme 2d indicates that the average crystal size of the (4F-PEA)(PPA)PbI_4/$MAPbI_3$ bilayer thin film is larger than that of the $(PPA)_2PbI_4$/$MAPbI_3$ bilayer thin film, which is larger than that of the $(4F\text{-}PEA)_2PbI_4$/$MAPbI_3$ bilayer thin film. Large crystal size could boost the charge transport, resulting in enhanced charge carrier mobility. In addition, as indicated in Figure 4a, among these three 2D/3D MHPs bilayer thin films, the smallest trap density observed from the (4F-PEA)(PPA)PbI_4/$MAPbI_3$ bilayer thin film illustrates that the (4F-PEA)(PPA)PbI_4/$MAPbI_3$ bilayer thin film has the highest charge carrier mobility.

It is found that the (4F-PEA)(PPA)PbI_4/$MAPbI_3$ bilayer thin film possesses a tendance of balanced charge transport (μ_e/μ_h = 0.69) compared to the $(4F\text{-}PEA)_2PbI_4$/$MAPbI_3$ thin film (μ_e/μ_h = 0.22) and the $(PPA)_2PbI_4$/$MAPbI_3$ (μ_e/μ_h = 0.54) bilayer thin film as well. Such balanced charge transport is attributed to the reduced crystal imperfections and binary conjugated organic cations. Thus, the PSCs and PPDs based on the 2D/3D MHPs bilayer thin films with a balanced charge transport are expected to exhibit a boosted short-circuit current (J_{SC}).

Based on $N_t = (2\varepsilon_0\varepsilon V_{TFL})/(eL^2)$ (where N_t is the trap density, L is the thickness of the active layer, ε_0 is the vacuum permittivity (8.85×10^{-12} C V^{-1} m^{-1}), ε is the relative dielectric constant of the active layer, e is the elementary electric charge, and V_{TFL} is the trap-filled limit voltage, respectively), N_t for the $(4F\text{-}PEA)_2PbI_4$/$MAPbI_3$, $(PPA)_2PbI_4$/$MAPbI_3$, and (4F-PEA)(PPA)PbI_4/$MAPbI_3$ bilayer thin films could be estimated. V_{TFL} for the hole-only diodes based on the $(4F\text{-}PEA)_2PbI_4$/$MAPbI_3$, $(PPA)_2PbI_4$/$MAPbI_3$, and (4F-PEA)(PPA)PbI_4/$MAPbI_3$ bilayer thin films are 0.98, 0.95, and 0.90 V, respectively. As a result, the electron-trap densities of 2.34×10^{16}, 2.20×10^{16}, and 2.04×10^{16} cm^{-3} are estimated for the $(4F\text{-}PEA)_2PbI_4$/$MAPbI_3$, $(PPA)_2PbI_4$/$MAPbI_3$, and (4F-PEA)(PPA)PbI_4/$MAPbI_3$ bilayer thin films, respectively. V_{TFL} for the electron-only diodes based on the $(4F\text{-}PEA)_2PbI_4$/$MAPbI_3$, $(PPA)_2PbI_4$/$MAPbI_3$, and (4F-PEA)(PPA)PbI_4/$MAPbI_3$ bilayer thin films are 0.95, 0.62 and 0.57 V, respectively. Thus, the estimated electron-trap densities of 2.26×10^{16}, 1.44×10^{16}, and 1.29×10^{16} cm^{-3} are for the $(4F\text{-}PEA)_2PbI_4$/$MAPbI_3$, $(PPA)_2PbI_4$/$MAPbI_3$, and (4F-PEA)(PPA)PbI_4/$MAPbI_3$ bilayer thin films, respectively. Therefore, both hole- and electron-trap densities for the (4F-PEA)(PPA)PbI_4/$MAPbI_3$ bilayer thin film are suppressed with, respectively, those for the $(4F\text{-}PEA)_2PbI_4$/$MAPbI_3$ and $(PPA)_2PbI_4$/$MAPbI_3$ bilayer thin films. Such reduced traps for the (4F-PEA)(PPA)PbI_4/$MAPbI_3$ bilayer thin film (Scheme 2) are probably ascribed to the suppressed point defects at the atomic scale and enlarged crystal grain size with fewer grain boundaries.

Both absorption and photoluminescent (PL) spectroscopies of the 2D/3D MHPs bilayer thin films are shown in Figure 2a,b. For better discussion of the bandgap of the 2D perovskites, the Tauc plot is plotted. No significant difference is observed from these three different 2D/3D MHPs bilayer thin films, indicating that the bandgaps of these three different 2D MHPs are nearly identical. Moreover, these three different 2D/3D MHPs bilayer thin films exhibit the same PL spectra under the light illuminated from the back side (through the glass substrate) of the 2D/3D MHPs bilayer thin films (Figure S2). These results demonstrate that PL is emitted from the 3D MHPs thin film, which further confirms that the 2D MHPs are formed on top of the 3D MHPs thin film. However, as the illumination light is directly on the surface (from the front side) of the 2D/3D MHPs bilayer thin films, three different 2D/3D MHPs bilayer thin films possess different PL intensities (Figure 2b). Compared to the $(4F\text{-}PEA)_2PbI_4$/$MAPbI_3$ bilayer thin film, an intense PL from the $(PPA)_2PbI_4$/$MAPbI_3$ bilayer thin film indicates a weaker interfacial nonradiative charge carrier recombination occurred, which is attributed to conjugated organic cation PPA.[35] Furthermore, compared to the $(PPA)_2PbI_4$/$MAPbI_3$ bilayer thin film, a more intense PL observed from the (4F-PEA)(PPA)PbI_4/$MAPbI_3$ bilayer thin film illustrates that a significantly suppressed interfacial nonradiative charge carrier recombination occurs in the (4F-PEA)(PPA)PbI_4/$MAPbI_3$ bilayer thin film. Thus, the PSCs and PPDs based on the (4F-PEA)(PPA)PbI_4/$MAPbI_3$ bilayer thin film are anticipated to exhibit an enhanced short-circuit current (J_{SC}).

To further understand the charge carrier recombination behavior and charge carrier dynamics in the 2D/3D MHPs bilayer thin films, both time-resolved PL (TR-PL) and transient absorption (TA) kinetics are investigated, and the results are shown in Figure 2c. The TR-PL results are fitted by $\gamma = \gamma_0 + A_1e^{-t/\tau_1} + A_2e^{-t/\tau_2}$, which is an exponential decay function with the PL lifetime (τ_1, τ_2) and amplitudes (A_1, A_2). In this model, γ_0 is a constant, τ_1 represents the nonradiative charge carrier recombination induced by surface defects, and τ_2 represents the component of radiative recombination.[46,47] The estimated τ_1 for the (4F-PEA)(PPA)PbI_4/$MAPbI_3$, $(PPA)_2PbI_4$/$MAPbI_3$, and $(4F\text{-}PEA)_2PbI_4$/$MAPbI_3$ bilayer thin films are 6.9, 7.4, and 9.6 ns (Figure 2c), respectively. The longer τ_1 is ascribed to the suppressed defect density within the 2D/3D MHPs bilayer thin films. Among these three different 2D/3D MHPs bilayer thin films, the longest τ_1 observed from the (4F-PEA)(PPA)PbI_4/$MAPbI_3$ bilayer thin film indicates that the surface defect is more pronounced suppressed than that of the $(PPA)_2PbI_4$/$MAPbI_3$ bilayer thin film. The surface defect within the $(4F\text{-}PEA)_2PbI_4$/$MAPbI_3$ bilayer thin film is less suppressed than that of the $(PPA)_2PbI_4$/$MAPbI_3$ bilayer thin film. Moreover, the estimated τ_2 for the (4F-PEA)(PPA)PbI_4/$MAPbI_3$, $(PPA)_2PbI_4$/$MAPbI_3$, and $(4F\text{-}PEA)_2PbI_4$/$MAPbI_3$ bilayer thin films are 16.6, 50.7, and 56.4 ns (Figure 2c), respectively. Compared to the $(4F\text{-}PEA)_2PbI_4$/$MAPbI_3$, a shorter τ_2 observed from the $(PPA)_2PbI_4$/$MAPbI_3$ indicates a more suppressed radiative recombination occurred compared with the $(4F\text{-}PEA)_2PbI_4$/$MAPbI_3$. A shorter τ_2 observed from (4F-PEA)(PPA)PbI_4/$MAPbI_3$ reveals that radiative recombination is suppressed compared to the $(PPA)_2PbI_4$/$MAPbI_3$. A shorter τ_2 and efficient charge extraction by the electrodes. Therefore, the (4F-PEA)(PPA)PbI_4/$MAPbI_3$ bilayer thin film possesses a remarkably suppressed nonradiative and radiative charge carrier recombination, which could result in a boosted J_{SC} for PPVs.

The TA kinetics for the 2D/3D MHPs bilayer thin films are shown in Figure 2d. All 2D/3D MHPs bilayer thin films exhibit two decay components: the first fast decay (τ_1) and the

https://doi.org/10.1021/acsami.4c00288
ACS Appl. Mater. Interfaces 2024, 16, 19318−19329

Scheme 3. (a) Device Structure of PSCs and (b) LUMO and HOMO Energy Levels of Materials and the WFs of the Electrodes Used for the Fabrication of PSCs

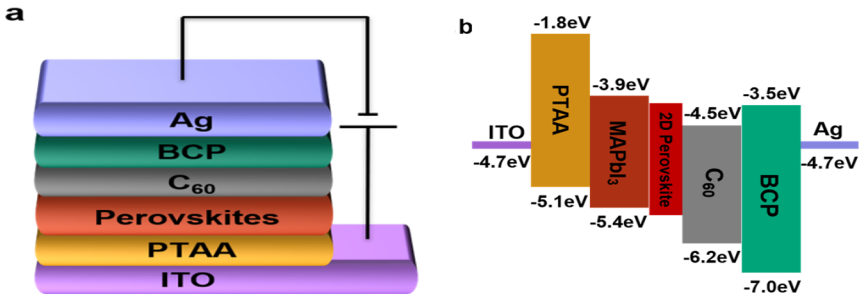

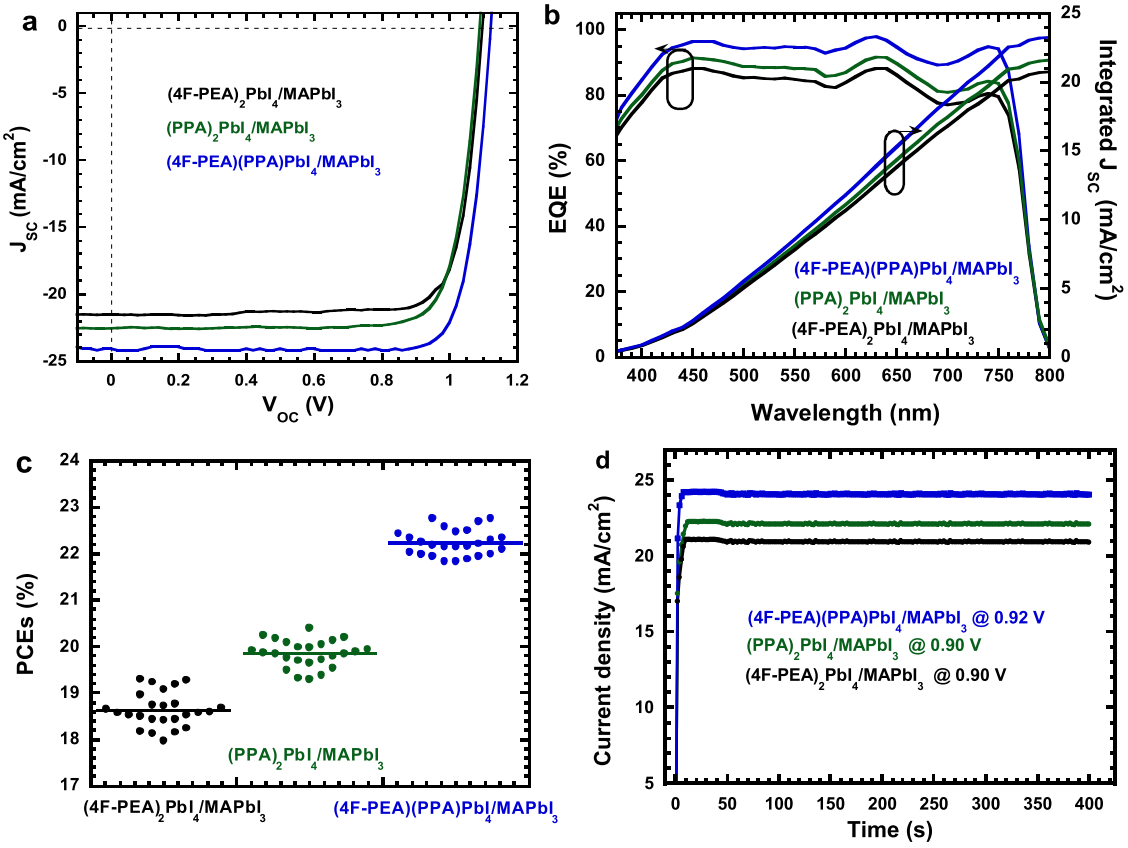

Figure 3. (a) J–V characteristics, (b) EQE spectra, (c) statistical distribution of reported PCEs, and (d) stabilized power output (SPO) J_{SC} versus the time of PSCs, where the PSCs are based on the $(4F\text{-}PEA)_2PbI_4/MAPbI_3$, $(PPA)_2PbI_4/MAPbI_3$, and $(4F\text{-}PEA)(PPA)PbI_4/MAPbI_3$ bilayer thin films, respectively.

second long decay (τ_2). For the 2D/3D MHPs bilayer thin films, surface passivation and large grain size could slow down both decay processes.[47−50] By fitting the TA kinetics, τ_1 of 0.7 ns (35% by weight ratio), 0.8 ns (38% by weight ratio), and 1.1 ns (26% by weight ratio) are observed from the $(4F\text{-}PEA)_2PbI_4/MAPbI_3$, $(PPA)_2PbI_4/MAPbI_3$ and $(4F\text{-}PEA)(PPA)PbI_4/MAPbI_3$ bilayer thin films, respectively. Moreover, τ_2 of 6.8 ns (65% by weight ratio), 7.0 ns (62% by weight ratio), and 7.9 ns (74% by weight ratio) are observed from the $(4F\text{-}PEA)_2PbI_4/MAPbI_3$, $(PPA)_2PbI_4/MAPbI_3$, and $(4F\text{-}PEA)(PPA)PbI_4/MAPbI_3$ bilayer thin films, respectively. Among these three different 2D/3D bilayer MHPs thin films, the $(4F\text{-}PEA)(PPA)PbI_4/MAPbI_3$ bilayer thin film has the longest τ_1 and τ_2 values, indicating that the $(4F\text{-}PEA)(PPA)PbI_4/MAPbI_3$ bilayer thin film possesses dramatically suppressed nonradiative charge carrier recombination. As a result, the PSCs and PPDs based on the $(4F\text{-}PEA)(PPA)PbI_4/MAPbI_3$ bilayer thin film should have boosted J_{SC}.

In addition, bleaching occurred in the ground state at ∼750 nm shown in the pseudocolor TA spectra (TAS) of the 2D/3D MHPs bilayer thin films (Figure S3) suggests that the photoexcited electrons located in the excited state, and the holes located in the ground state could reduce the absorption of probed photons because of photoinduced charge transfer occurred in these MHPs bilayer thin films.[51] The bandgap of 2D MHPs is slightly wider than that of 3D MHPs (Scheme 3b), and the 2D/3D MHPs bilayer thin films could form a classical type-I heterojunction. In typical PPVs based on the 3D MHPs, the charge carrier recombination mainly occurs at the interface between the 3D MHPs and the electrodes, where the charge carriers are trapped by the surface defects.[52,53] The type-I heterojunction formed between 2D MHPs and 3D

https://doi.org/10.1021/acsami.4c00288
ACS Appl. Mater. Interfaces 2024, 16, 19318−19329

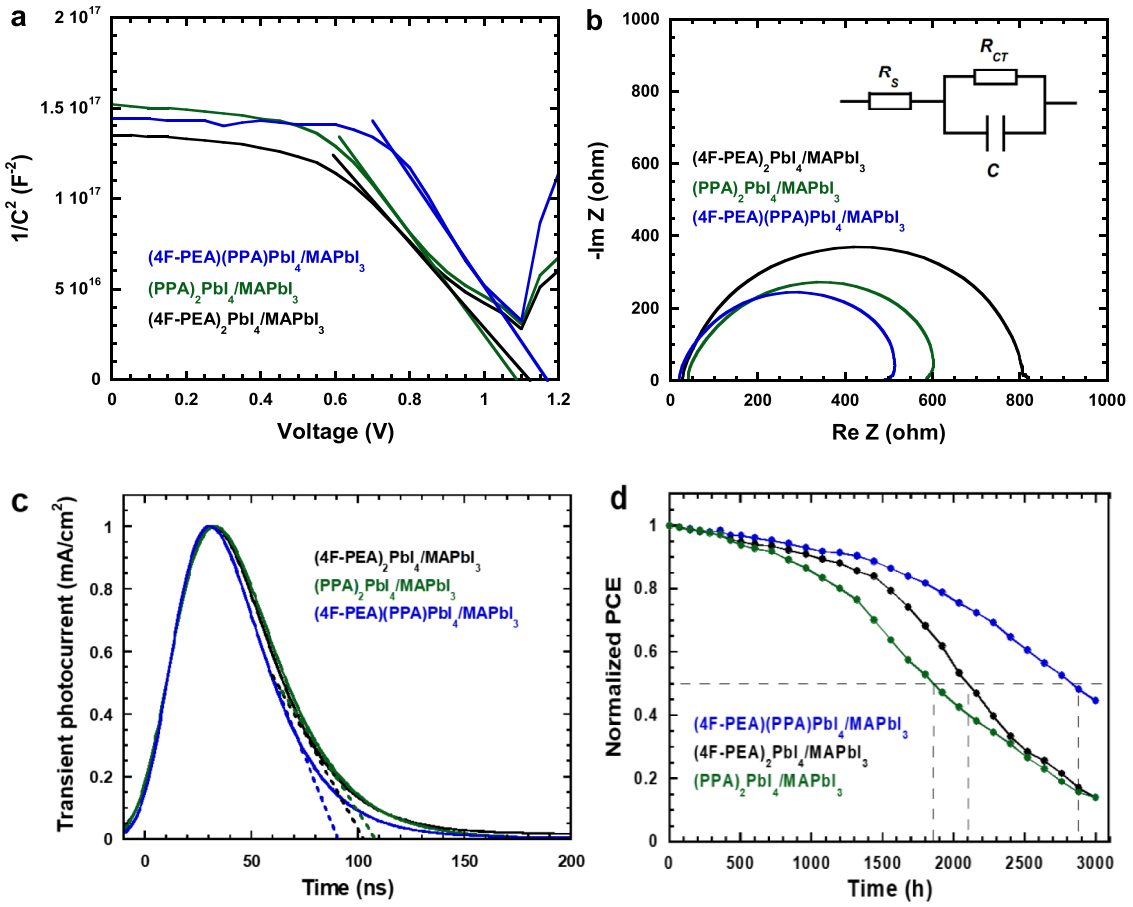

Figure 4. (a) C−V characteristics and (b) impedance spectra of the PSCs, (c) normalized transient photocurrent (TPC) curves of PSCs, and (d) shelf-stability of unencapsulated PSCs tested in the air with a ∼25% relative humidity at RT, where the PSCs are based on the $(4F\text{-}PEA)_2PbI_4/MAPbI_3$, $(PPA)_2PbI_4/MAPbI_3$, and $(4F\text{-}PEA)(PPA)PbI_4/MAPbI_3$ bilayer thin films.

MHPs has two functionalities. One is to allow photoinduced charge carrier transfer from 3D MHPs to 2D MHPs, which could result in a long lifetime decay for the 2*D*/3D MHPs bilayer thin films. Such photoinduced charge transfer could result in a boosted J_{SC} for PSCs and PPDs. Another is to restrict the charge transport from 2D MHPs to 3D MHPs, resulting in an enlarged J_{SC} for PSCs and PPDs as well. Therefore, the PSCs and PPDs based on the $(4F\text{-}PEA)(PPA)PbI_4/MAPbI_3$ bilayer thin film exhibit the highest J_{SC} compared to those based on the $(4F\text{-}PEA)_2PbI_4/MAPbI_3$ and $(PPA)_2PbI_4/MAPbI_3$ bilayer thin films.

A device structure of ITO/PTAA/MHPs/C_{60}/BCP/Ag (Scheme 3a), where ITO (indium tin oxides) acts as the anode, PTAA (poly[bis(4-phenyl)(2,4,6-trimethylphenyl)-amine] acts as the hole extraction layer (HEL), MHPs are the 2D/3D MHPs bilayer thin films, C_{60} is used as the EEL, BCP (bathocuproine) acts as the hole blocking layer (HBL), and Ag (silver) acts as the cathode, respectively, is used to evaluate PSCs device performance. The work functions (WFs) of the ITO and Ag electrodes and the lowest occupied molecular orbital (LUMO) and the highest occupied molecular orbital (HOMO) energy levels of the PTAA HEL, 2D MHPs, 3D MHPs, C_{60} EEL, and BCP HBL are displayed in Scheme 3b. The 2D MHPs possess a winder bandgap compared to their corresponding 3D MHPs, which is due to the quantum confinement.[53,54] Thus, the 2D MHPs are anticipated to have a slightly lower LUMO energy level compared with that of 3D MHPs. The HOMO energy level (−5.1 eV) of the PTAA HEL is higher than that (−5.4 eV) of 3D MHPs, the latter is slightly higher than that of 2D MHPs but is below the WF (−4.7 eV) of the ITO anode. The energy-level alignment shown in Scheme 3b could ensure the separated holes are transferred from the 2D/3D MHPs bilayer thin film to the PTAA HEL and then collected by the ITO anode.[55,56] On the other hand, the LUMO energy level (−4.5 eV) of the C_{60} EEL is lower than that of 2D MHPs, which is lower than that (−3.9 eV) of 3D MHPs but is higher than the WF (−4.7 eV) of the Ag cathode.[57,58] Such energy-level alignment could also ensure that the separated electrons are transferred from the 2D/3D MHPs bilayer into the C_{60} EEL and then collected by the Ag cathode. Moreover, the BCP HBL with a deep HOMO level could ensure the separated holes are blocked from the photoactive layer, preventing back transfer. The PSCs with a device architecture as shown in Scheme 3a could ensure that efficient charge association and disassociation take place in the 2*D*/3D MHPs bilayer thin film. Therefore, a boosted J_{SC} is anticipated from PSCs.

The current density versus voltage (J−V) characteristics of PSCs are shown in Figure 3a. The $(4F\text{-}PEA)_2PbI_4/MAPbI_3$-based PSCs exhibit an open-circuit voltage (V_{OC}) of 1.10 V, a J_{SC} of 21.52 mA/cm^2, a fill factor (FF) of 0.82, and a corresponding PCE of 19.40%. The $(PPA)_2PbI_4/MAPbI_3$-based PSCs exhibit a V_{OC} of 1.09 V, a J_{SC} of 22.54 mA/cm^2, an FF of 0.83, and a corresponding PCE of 20.39%. All these device performance parameters are consistent with previous reports.[5,35] The $(4F\text{-}PEA)(PPA)PbI_4/MAPbI_3$-based PSCs

https://doi.org/10.1021/acsami.4c00288
ACS Appl. Mater. Interfaces 2024, 16, 19318−19329

exhibit a V_{OC} of 1.12 V, a J_{SC} of 24.19 mA/cm^2, an FF of 0.84, with a corresponding PCE of 22.76%, which is a more than 10% enhancement compared to that based on the $(PPA)_2PbI_4/MAPbI_3$ bilayer thin film, and is an approximatively 20% enhancement compared to that based on the $(4F\text{-}PEA)_2PbI_4/MAPbI_3$ bilayer thin film.

Moreover, the PSCs based on the $(4F\text{-}PEA)(PPA)PbI_4/MAPbI_3$ bilayer thin films possess improved external quantum efficiency (EQE) values from 400 to 780 nm compared to those based on the $(4F\text{-}PEA)_2PbI_4/MAPbI_3$ and $(PPA)_2PbI_4/MAPbI_3$ bilayer thin films, respectively (Figure 3b). The enhanced EQE values are attributed to the suppressed trap density. In addition, based on EQE = $(J_{SC}/q)/(P_0\lambda/hc)$, where q is the elementary charge, P_0 is the light intensity (100 mW/cm^2), λ is the wavelength, h is the Planck constant, c is the light speed in a vacuum, the photocurrent, termed as the integrated J_{SC}, could be obtained. The integrated J_{SC} values are 20.76, 21.60, and 23.24 mA/cm^2 for the PSCs based on the $(4F\text{-}PEA)_2PbI_4/MAPbI_3$, $(PPA)_2PbI_4/MAPbI_3$, and $(4F\text{-}PEA)(PPA)PbI_4/MAPbI_3$ bilayer thin films, respectively. These integrated J_{SC} values are in good agreement with those observed from the J−V characteristics (Figure 3a).

The derivations in PCEs for each type of PSCs are around ±10% (Figure 3c). The corresponding J_{SC} distribution is shown in Figure S4. The PCEs observed from the PSCs based on the $(4F\text{-}PEA)(PPA)PbI_4/MAPbI_3$ bilayer thin film have a narrowed distribution factor compared to those based on the $(4F\text{-}PEA)_2PbI_4/MAPbI_3$ and $(PPA)_2PbI_4/MAPbI_3$ bilayer thin films, respectively, which indicates that the reproducibility of the PSCs based on the $(4F\text{-}PEA)(PPA)PbI_4/MAPbI_3$ bilayer thin film is higher than those based on the $(4F\text{-}PEA)_2PbI_4/MAPbI_3$ and $(PPA)_2PbI_4/MAPbI_3$ bilayer thin films, respectively. Such high reproducibility is attributed to the superior film morphology of the $(4F\text{-}PEA)(PPA)PbI_4/MAPbI_3$ thin film.

To determine the consistency of PCEs, the stabilized power output (SPO) testing is conducted at the bias of 0.90, 0.90, and 0.92 V for the PSCs based on the $(4F\text{-}PEA)(PPA)PbI_4/MAPbI_3$, $(PPA)_2PbI_4/MAPbI_3$, and $(4F\text{-}PEA)_2PbI_4/MAPbI_3$ bilayer thin films, respectively, and the results are shown in Figure 3d. The PSCs based on the $(4F\text{-}PEA)(PPA)PbI_4/MAPbI_3$ bilayer thin film shows a faster stabilized J_{SC} than that based on the $(PPA)_2PbI_4/MAPbI_3$ bilayer thin film, which exhibits a faster stabilized J_{SC} than that based on the $(4F\text{-}PEA)_2PbI_4/MAPbI_3$ bilayer thin film. The faster stabilized J_{SC} indicates that the trap-assisted charge carrier recombination is suppressed, which is attributed to the reduced trap density with the 2D/3D MHPs bilayer thin film. Moreover, the stabilized PCEs for the PSCs based on the $(4F\text{-}PEA)(PPA)PbI_4/MAPbI_3$, $(PPA)_2PbI_4/MAPbI_3$, and $(4F\text{-}PEA)_2PbI_4/MAPbI_3$ bilayer thin films are 22.20, 19.81, and 18.68%, respectively, which correspond to 97.9, 97.1, and 96.2% of their PCEs under the reverse scan direction, respectively (Figure S5). The higher SPO ratio indicates that PSCs based on the $(4F\text{-}PEA)(PPA)PbI_4/MAPbI_3$ bilayer thin film have a more pronounced suppressed nonradiative charge carrier recombination.

Figure 4a shows the capacitance versus voltage (C−V) characteristics of the PSCs. Based on $C^2 = q\varepsilon_0\varepsilon N_A/2(V_0 - V)$[53] (where q is the elementary charge (1.6×10^{-19} C), N_A is the trap density, V_0 is the built-in potential, V is the applied voltage, ε_0 is the vacuum permittivity (which is 8.55×10^{-12} F m^{-1}), and ε is the dielectric constant (Figure S1), respectively), the trap density of PSCs, which is directly related to the slop of the C−V curves, could be estimated. After the linear fitting, the trap densities are estimated to be 2.6×10^{16}, 2.0×10^{16}, and 1.7×10^{16} for the PSCs based on the $(4F\text{-}PEA)_2PbI_4/MAPbI_3$, $(PPA)_2PbI_4/MAPbI_3$, and $(4F\text{-}PEA)(PPA)PbI_4/MAPbI_3$ bilayer thin films, respectively. The large absolute slope value indicates the small interfacial charge carrier density within the PSCs. Thus, the charge carrier recombination is more pronounced suppressed in the PSCs based on the $(4F\text{-}PEA)(PPA)PbI_4/MAPbI_3$ bilayer thin film as compared to those based on the $(4F\text{-}PEA)_2PbI_4/MAPbI_3$ and $(PPA)_2PbI_4/MAPbI_3$ bilayer thin films. As a result, the PSCs based on the $(4F\text{-}PEA)(PPA)PbI_4/MAPbI_3$ bilayer thin film exhibit a larger J_{SC}. On the other hand, the built-in potential (V_{bin}) values could be observed from the intercept in the x-axis (Figure 4a). The V_{bin} values are 1.12, 1.08, and 1.17 V for the PSCs based on the $(4F\text{-}PEA)_2PbI_4/MAPbI_3$, $(PPA)_2PbI_4/MAPbI_3$, and $(4F\text{-}PEA)(PPA)PbI_4/MAPbI_3$ bilayer thin films, respectively. As a result, a larger V_{OC} is observed from the PSCs based on the $(4F\text{-}PEA)(PPA)PbI_4/MAPbI_3$ bilayer thin film compared to those based on the $(4F\text{-}PEA)_2PbI_4/MAPbI_3$ and $(PPA)_2PbI_4/MAPbI_3$ bilayer thin films.

The impedance spectroscopy (IS) study is further carried out to measure the specific electrical properties, such as inner series resistance (R_S), of the 2D/3D MHPs bilayer thin films, which are difficult to directly measure. Based on the electric circuit model (inset of Figure 4b), R_S is the sum of sheet resistance (R_{Sheet}) and charge-transfer resistance (R_{CT}). R_{Sheet} is the resistance of the electrodes, R_{CT} is the resistance of the interface including the resistance between the PTAA HEL and the ITO anode, the resistance between the C_{60} EEL and the Ag cathode, the resistance between the 2D/3D MHPs bilayer thin film and charge transfer layer (HEL or EEL).[43] R_{CT} observed from the PSCs based on the $(4F\text{-}PEA)(PPA)PbI_4/MAPbI_3$ bilayer thin film is 511 Ω, which is smaller than that (603 Ω) from the PSCs based on the $(PPA)_2PbI_4/MAPbI_3$ bilayer thin film. The latter is smaller than that (808 Ω) observed from the PSCs based on the $(4F\text{-}PEA)_2PbI_4/MAPbI_3$ bilayer thin film. The role of the conjugated organic spacer in boosting charge carrier transport and minimizing transfer resistances, leading to a higher FF for the PSCs, is demonstrated clearly by lower R_{CT} from the cells.[59] As a result, a larger J_{SC} is observed from the PSCs based on the $(4F\text{-}PEA)(PPA)PbI_4/MAPbI_3$ bilayer thin film compared to those based on the $(PPA)_2PbI_4/MAPbI_3$ and $(4F\text{-}PEA)_2PbI_4/MAPbI_3$ bilayer thin films.

To figure out the charge generation and transport kinetics in PSCs, the transient photocurrent (TPC) measurement is conducted.[42,60] It is found that the extracted charge carrier densities of the PSCs based on the $(4F\text{-}PEA)(PPA)PbI_4/MAPbI_3$ bilayer thin film are higher compared to those based on either $(PPA)_2PbI_4/MAPbI_3$ or $(4F\text{-}PEA)_2PbI_4/MAPbI_3$ bilayer thin films (Figure S6), which confirm that the PSCs based on the $(4F\text{-}PEA)(PPA)PbI_4/MAPbI_3$ bilayer thin film exhibit the highest J_{SC} among these three different PSCs. Moreover, the TPC curves exhibit a linear region before 30 ns, which is ascribed to the short time of charge carrier extraction.[42,61] After that, due to the trap and detrap processes of the charge carriers, these three different PSCs exhibit different time scales. As indicated in Figure 4c, the PSCs based on the $(4F\text{-}PEA)(PPA)PbI_4/MAPbI_3$ bilayer thin film possess a charge transfer lifetime of ∼90 ns, while the PSCs based on the $(PPA)_2PbI_4/MAPbI_3$ and $(4F\text{-}PEA)_2PbI_4/MAPbI_3$ bilayer thin films have the lifetime of ∼100 and ∼110 ns, respectively.

https://doi.org/10.1021/acsami.4c00288
ACS Appl. Mater. Interfaces 2024, 16, 19318−19329

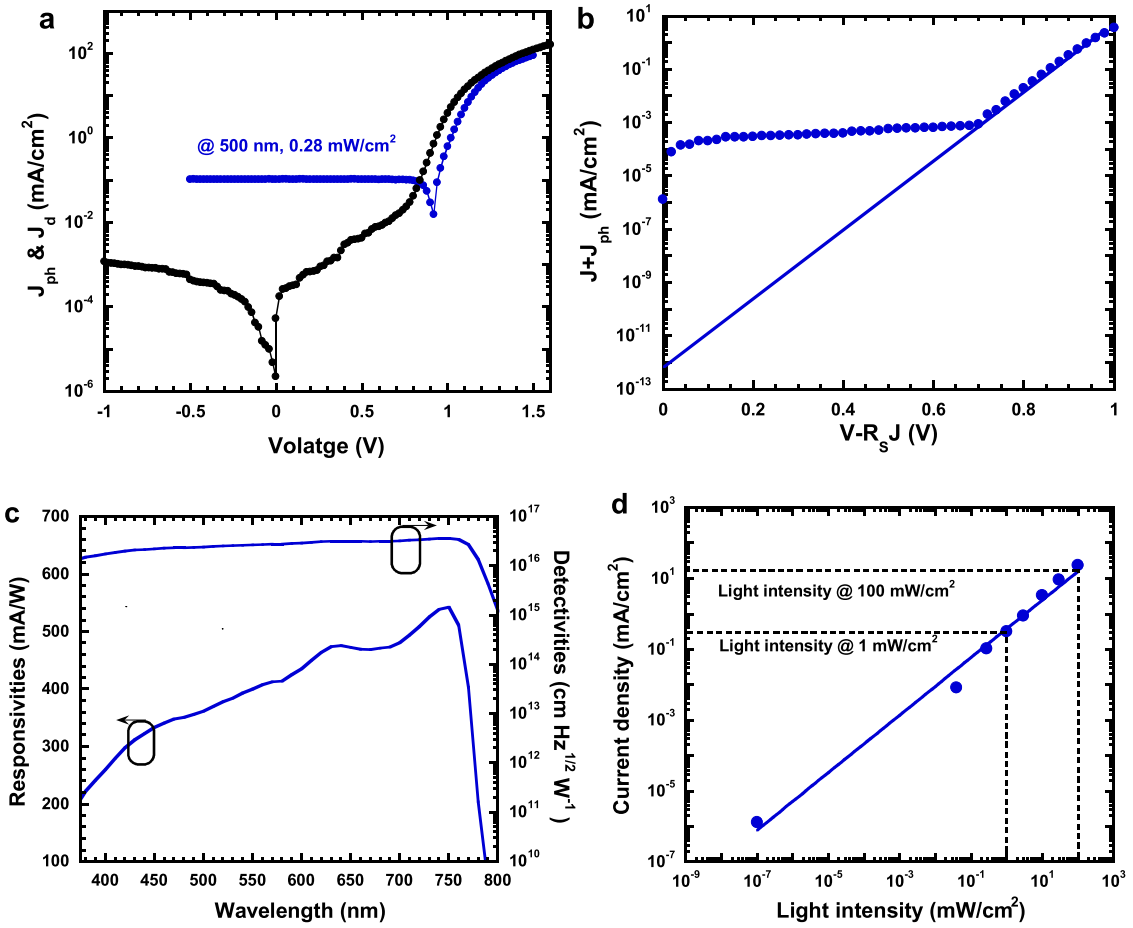

Figure 5. (a) J–V characteristics of the PPDs under monochromatic light at a wavelength of 500 nm with the light intensity of 0.28 mW/cm^2 and in the dark tested at RT, (b) $\ln(J + J_{ph})$ versus $(V - R_S T)$ and the linear fitting, (c) responsivities and detectivities of the PPDs, and (d) linear dynamic range of the PPDs, where the PPDs are based on the (4F-PEA)(PPA)PbI_4/$MAPbI_3$ bilayer thin film.

The shorter lifetime observed from the PSCs based on the (4F-PEA)(PPA)PbI_4/$MAPbI_3$ bilayer thin film indicates that the charge carrier is quickly swept out within PSCs,[61] resulting in a large J_{SC}. As a result, the PSCs based on the (4F-PEA)(PPA)PbI_4/$MAPbI_3$ bilayer thin films exhibit both enlarged J_{SC} and PCE compared to those based on the $(PPA)_2PbI_4$/$MAPbI_3$ and $(4F\text{-}PEA)_2PbI_4$/$MAPbI_3$ bilayer thin films.

Figure 4d shows the shelf stability of unencapsulated PSCs conducted at the maximum power point tested in the air with a ∼25% relative humidity at RT. The $(4F\text{-}PEA)_2PbI_4$/$MAPbI_3$-based PSCs show a significant degradation after it has been operated for ∼1350 h and can maintain 50% of their initial PCEs after 2100 h operation. Under the same condition, the $(PPA)_2PbI_4$/$MAPbI_3$-based PSCs show a significant degradation after they have been tested for ∼1200 h and can maintain 50% of their initial PCEs after 1800 h operation, whereas the (4F-PEA)(PPA)PbI_4/$MAPbI_3$-based PSCs show a degradation after it has been tested for ∼1600 h and can maintain 50% of their initial PCEs after 2900 h operation. These results demonstrate that the PSCs based on the (4F-PEA)(PPA)PbI_4/$MAPbI_3$ bilayer thin film possess boosted stability compared to those based on the $(PPA)_2PbI_4$/$MAPbI_3$ and $(4F\text{-}PEA)_2PbI_4$/$MAPbI_3$ bilayer thin films. Such enhanced stability is ascribed to the binary conjugated organic cations, which could better anchor the grain boundary of MHPs and withstand moisture and oxygen.

The PPDs based on the (4F-PEA)(PPA)PbI_4/$MAPbI_3$ bilayer thin film with the same device structure as that shown in Scheme 3a are also investigated. Figure 5a shows the J–V characteristics of PPDs measured in the dark and under monochromatic light at a λ of 500 nm with a light intensity of 0.28 mW/cm^2, operated at RT. According to $J = J_0[\exp(q(V - JR_S)/nk_bT) - 1] - J_{ph}$ (where J is the total current density and J_{ph} is the photocurrent (from the J–V curves as shown in Figure 5a), V is the applied voltage, q is the elementary charge, R_S is the series resistance, n is the idea factor, k_b is the Boltzmann constant, and T is the absolute temperature), the saturated dark current density (J_0) could be obtained.[62] Figure 5b shows the $\ln(J_{ph} + J)$ versus the $(V - R_S J)$ curve and the linear fittings. Thus, J_0 is calculated to be 7.01×10^{-13} mA/cm^2. Thus, the PPDs based on the (4F-PEA)(PPA)PbI_4/$MAPbI_3$ bilayer thin film exhibit a very low dark current density, which implies that PPDs could possess large projected detectivities (D^*).[61] Based on the EQE spectra (Figure 3b), the responsivity (R), described as $R = EQE \times \lambda/1240$, could be calculated. The R values versus the wavelengths of PPDs are shown in Figure 5c. The PPDs based on the (4F-PEA)(PPA)-PbI_4/$MAPbI_3$ bilayer thin film possess high R. For example, at λ = 500 nm, the R value is 370 A/mW.

According to $D^* = R/(2qJ_d)^{1/2}$,[63] the D^* versus wavelength is obtained, and the results are shown in Figure 5c. Ranging from 400 to 800 nm, the PPDs based on the (4F-PEA)(PPA)PbI_4/$MAPbI_3$ bilayer thin film exhibit over 10^{16}

https://doi.org/10.1021/acsami.4c00288
ACS Appl. Mater. Interfaces 2024, 16, 19318−19329

Jones D^*, which is higher than those observed from the PPDs based on the 3D MHPs thin film[64] and/or the PEA_2PbI_4/$MAPbI_3$ bilayer thin film as well.[65]

Figure 5d presents the linear dynamic range (LDR) of the PPDs. The LDR or photosensitivity linearity (typically quoted in dB), defined as LDR = $20\log(J^*_{ph}/J^*_d)$, where J^*_0 is the dark current at 0 V, J^*_{ph} is the photocurrent density measured at the light intensity of 1 mW cm^{-2}, is another key parameter used to evaluate the device performance of PPDs.[62,66] At RT, the LDR is calculated to be 108 dB, which is higher than the (91 dB) observed from the PPDs based on the 3D $MAPbI_3$ thin film. Such large LDR is comparable to that of Si-based PDs (120 dB, at 77 K) and is significantly higher than that (66 dB, at 4.2 K) of InGaAs-based PDs.[67]

3. CONCLUSIONS

In conclusion, we reported the development of binary conjugated organic cation-based 2D MHPs and further demonstrated stable and efficient PSCs and ultrasensitive PPDs. Compared to the $(4F\text{-}PEA)_2PbI_4$/$MAPbI_3$ and $(PPA)_2PbI_4$/$MAPbI_3$ bilayer thin films, the (4F-PEA)(PPA)-PbI_4/$MAPbI_3$ bilayer thin film possessed enlarged crystals, suppressed charge carrier recombination, balanced charge transport, smaller charge-transfer resistance, and faster charge-extraction transfer process. As a result, the PSCs based on the (4F-PEA)(PPA)PbI_4/$MAPbI_3$ bilayer thin film exhibited a PCE of 22.76%, which was an approximately 20% enhancement compared to that based on the $(4F\text{-}PEA)_2PbI_4$/$MAPbI_3$ bilayer thin film. Compared to the PSCs based on the $(PPA)_2PbI_4$/$MAPbI_3$ bilayer thin film, more than 10% boosted PCEs were observed from the PSCs based on the (4F-PEA)(PPA)PbI_4/$MAPbI_3$ bilayer thin film. Moreover, unencapsulated PSCs based on the (4F-PEA)(PPA)PbI_4/$MAPbI_3$ bilayer thin film tested at the maximum power point possessed 50% of their initial PCEs for 2900 h of operation in the air with a ∼25% relative humidity. In addition, the PPDs based on the (4F-PEA)(PPA)PbI_4/$MAPbI_3$ bilayer thin film possessed a projected detectivity of 10^{16} Jones and a linear dynamic range of 108 dB at room temperature. All of these results indicated that we provided a facile way to approach high-performance PSCs and PPDs.

4. EXPERIMENTAL SECTION

4.1. Materials. Gamma-butyrolactone (GBL, 99%), 4-fluorophenethylammonium iodide (*4F*-PEAI, 99%), 1-butanol (99.7%), anhydrous toluene (99.8%), methylamine (33 wt % in absolute ethanol), anhydrous acetonitrile (ACN, 99.8%), poly[bis(4-phenyl)-(2,4,6-trimethylphenyl)amine (*PTAA*), [2-(3,6-dimethoxy-9*H*-carbazol-9-yl)ethyl]phosphonic acid (MeO-2PACz), molybdenum oxide (MoO_3), silver (Ag), tin oxides (SnO_2), [6,6] phenyl-C_{61}-butyric acid methyl ester ($PC_{61}BM$), and bathocuproine (BCP) were purchased from Sigma-Aldrich. Lead iodide (PbI_2, 99.9985% metal basis) was purchased from Alfa Aesar. Methylammonium iodide (CH_3NH_3I (MAI)) was purchased from Greatcell Solar Materials. All materials were used as received without further processing. 3-phenyl-2-propen-1-amine (PPA) was synthesized as we previously reported.[35]

4.2. Preparation of $MAPbI_3$ Single Crystals and $MAPbI_3$ ACN Solution. The inverse temperature crystallization method was used to synthesize the $MAPbI_3$ single crystals.[65] 1 mmol PbI_2 mixed with 1 mmol MAI was added into 1 mL GBL solvent and then heated and stirred continually until they were completely dissolved, and their color was changed to a clear yellow. Afterward, the solution was kept at 110 °C allowing the $MAPbI_3$ single crystals to grow naturally. After 12 h (h), the shape-regular black-color single crystals were formed. These crystals were washed with isopropanol (IPA) and then dried in the oven for 10 min (min).

The $MAPbI_3$ ACN solution was prepared as we reported previously.[65] Briefly, the $MAPbI_3$ single crystals were placed into a small vial with an opened cap, which was seated inside a large vial with a certain amount of methylamine ethanol solution. In this way, the $MAPbI_3$ single crystals could be exfoliated by methylamine vapor to generate a viscous yellowish solution. Afterward, a 1 mol/L $MAPbI_3$ ACN precursor solution was obtained by adding ACN into the above viscous yellowish solution.

4.3. Preparation and Characterization of the 2D/3D MHPs Bilayer Thin Films. The PPA mixed with 4F-PEA precursor solution was prepared by dissolving their mixed powders into a butanol solvent. $MAPbI_3$, $(4F\text{-}PEA)_2PbI_4$/$MAPbI_3$, $(PPA)_2PbI_4$/$MAPbI_3$, and (4F-PEA)(PPA)PbI_4/$MAPbI_3$ bilayer thin films were prepared by the method as we previously reported.[19,35,65]

The top-view SEM images of the 2D/3D MHPs bilayer thin films were conducted on a field-emission SEM (JEOL-7401). The HP 8453 spectrophotometer was used to acquire the absorption spectra of the 2D/3D MHPs bilayer thin films. The PL spectra were conducted on the HORIBA Fluorolog-3 fluorescence spectrophotometer in the air. The excitation wavelength was set at 530 nm. During the PL measurement, the homogeneous 2D/3D MHPs bilayer thin films with a similar thickness were placed in the exact position for comparison studies. To detect the time-resolved PL trace, a pulsed source at 400 nm (Horiba Deltadiode) is used as excitation, and the signal is recorded at 750 nm by the time-correlated single-photon counting detection (Horiba PPD850). The transient absorption spectra were measured using the method reported in our previous publication.[50,51]

Charge carrier mobilities of the 2D/3D MHPs bilayer thin films were evaluated based on the SCLC method according to the Mott–Gurney model.[44,45]

4.4. Preparation and Characterization of PSCs and PPDs. The precleaned indium tin oxide (ITO) substrates were first processed by UV/ozone for 20 min (min) in an ambient environment and then transferred inside a glovebox with a nitrogen atmosphere. The ∼8 nm PTAA thin layer was first cast on the top of the ITO substrates. After that, the 3D $MAPbI_3$ thin film was spin-coated on the top of the PTAA thin layer. The $(4F\text{-}PEA)_2PbI_4$/$MAPbI_3$, $(PPA)_2PbI_4$/$MAPbI_3$, and (4F-PEA)(PPA)PbI_4/$MAPbI_3$ thin films were prepared as described in Section 4.3. Afterward, a ∼24 nm-thick C_{60}, a ∼6 nm BCP, and a ∼120 nm Ag were subsequently thermally deposited. The device area was measured to be 0.043 cm^2.

The details of PSCs and PPDs characterization are similar to and/or the same as those reported in our previous publications.[19,22,35,65,68]

■ ASSOCIATED CONTENT

Supporting Information

The Supporting Information is available free of charge at https://pubs.acs.org/doi/10.1021/acsami.4c00288.

Charge carrier mobilities of the 2D/3D MHPs bilayer thin films, photoluminescence spectra of the 2D/3D MHPs bilayer thin films, and characterization of perovskite photovoltaics (PDF)

■ AUTHOR INFORMATION

Corresponding Authors

He Wang − *Department of Physics, University of Miami, Coral Gables, Florida 33146, United States;* orcid.org/0000-0003-1365-0304; Email: hewang@miami.edu

Xiong Gong − *School of Polymer Science and Polymer Engineering, College of Engineering and Polymer Science and Department of Chemical, Biomolecular and Corrosion Engineering, College of Engineering and Polymer Science, The University of Akron, Akron, Ohio 44325, United States;* orcid.org/0000-0001-6525-3824; Email: xgong@uakron.edu

https://doi.org/10.1021/acsami.4c00288
ACS Appl. Mater. Interfaces 2024, 16, 19318−19329

Authors

Lening Shen − *School of Polymer Science and Polymer Engineering, College of Engineering and Polymer Science, The University of Akron, Akron, Ohio 44325, United States*

Haodong Wu − *School of Polymer Science and Polymer Engineering, College of Engineering and Polymer Science, The University of Akron, Akron, Ohio 44325, United States*

Zikun Cao − *Department of Physics, University of Miami, Coral Gables, Florida 33146, United States*

Xiyao Zhang − *School of Polymer Science and Polymer Engineering, College of Engineering and Polymer Science, The University of Akron, Akron, Ohio 44325, United States*

Lei Liu − *School of Polymer Science and Polymer Engineering, College of Engineering and Polymer Science, The University of Akron, Akron, Ohio 44325, United States*

Hussain Sawwan − *School of Polymer Science and Polymer Engineering, College of Engineering and Polymer Science, The University of Akron, Akron, Ohio 44325, United States*

Tao Zhu − *School of Polymer Science and Polymer Engineering, College of Engineering and Polymer Science, The University of Akron, Akron, Ohio 44325, United States;* orcid.org/0000-0001-9614-3476

Jie Zheng − *Department of Chemical, Biomolecular and Corrosion Engineering, College of Engineering and Polymer Science, The University of Akron, Akron, Ohio 44325, United States;* orcid.org/0000-0003-1547-3612

Complete contact information is available at: https://pubs.acs.org/10.1021/acsami.4c00288

Notes

The authors declare no competing financial interest.

■ ACKNOWLEDGMENTS

The authors acknowledge the National Science Foundation (NSF) (ECCS/EPMD1903303) and Air Force Office of Scientific Research (AFOSR) (through the Organic Materials Chemistry Program, grant no. FA9550-22-1-0488, Program Manager, Dr. Kenneth Caster) for financial supports.

■ REFERENCES

(1) Seo, J.; Noh, J. H.; Seok, S. I. Rational strategies for efficient perovskite solar cells. *Acc. Chem. Res.* **2016**, *49*, 562−572.

(2) Grätzel, M. The rise of highly efficient and stable perovskites solar cells. *Acc. Chem. Res.* **2017**, *50*, 487−491.

(3) Jena, A. K.; Kulkarni, A.; Miyasaka, T. Halide perovskite photovoltaics: background, status, and future, prospects. *Chem. Rev.* **2019**, *119*, 3036−3103.

(4) Huang, Y. M.; Lei, X. J.; He, T. W.; Jiang, Y. Z.; Yuan, M. J. Recent progress on formamidinium-dominated perovskite photovoltaics. *Adv. Energy Mater.* **2022**, *12*, No. 2100690.

(5) Shen, L.; Chen, R.; Zhang, D.; Yilmazoglu, U. C.; Gu, K.; Sarmiento, J. S.; Zhu, T.; Zheng, L.; Zheng, J.; Wang, H.; Liu, C. M.; Gong, X. High-performance perovskite photovoltaics by heterovalent substituted mixed perovskites. *Adv. Funct. Mater.* **2022**, *32*, No. 2207911.

(6) Yang, Y.; Wang, Y.; Qu, Z.; Zhang, K.; Liang, T.; Chen, S.; Lv, W.; Min, F.; Chen, Y.; Qiao, Y.; Song, Y. Volatile dual-solvent assisted intermediate phase regulation for anti-solvent-free perovskite photovoltaics. *Angew. Chem., Int. Ed.* **2023**, *62*, No. e202300971.

(7) Zheng, L.; Wang, K.; Zhu, T.; Liu, L.; Zheng, J.; Gong, X. Solution-processed ultrahigh detectivity photodetectors by hybrid perovskite incorporated with heterovalent neodymium cations. *ACS Omega* **2019**, *4*, 15873−15878.

(8) Zhu, T.; Shen, L.; Zhang, D.; Zheng, J.; Gong, X. Solution-processed ternary perovskite-organic broadband photodetectors with ultrahigh detectivity. *ACS Appl. Mater. Interfaces* **2022**, *14*, 18744−18750.

(9) Jiang, Q.; Tong, J.; Xian, Y.; Kerner, R. A.; Dunfield, S. P.; Xiao, C.; Scheidt, R. A.; Kuciauskas, D.; Wang, X.; Hautzinger, M. P.; Tirawat, R.; Beard, M. C.; Fenning, D. P.; Berry, J. J.; Larson, B. W.; Yan, Y.; Zhu, K. Surface reaction for efficient and stable inverted perovskite solar cells. *Nature* **2022**, *611*, 278−283.

(10) Park, J.; Kim, J.; Yun, H. S.; Paik, M. J.; Noh, E.; Mun, H. J.; Kim, M. G.; Shin, T. J.; Seok, S. Controlled growth of perovskite layers with volatile alkylammonium chlorides. *Nature* **2023**, *616*, 724−730.

(11) *Best Research-Cell Efficiency Chart, NREL*, https://www.nrel.gov/pv/cell-efficiency.html.

(12) Conings, B.; Drijkoningen, J.; Gauquelin, N.; Babayigit, A.; D'haen, J.; D'olieslaeger, L.; Ethirajan, A.; Verbeeck, J.; Manca, J.; Mosconi, E.; Angelis, F. D.; Boyen, H.-G. Intrinsic thermal instability of methylammonium lead trihalide perovskite. *Adv. Energy Mater.* **2015**, *5*, No. 1500477.

(13) Grancini, G.; Nazeeruddin, M. K. Dimensional tailoring of hybrid perovskites for photovoltaics. *Nat. Rev. Mater.* **2019**, *4*, 4−22.

(14) Boyd, C. C.; Cheacharoen, R. G.; Leijtens, T.; Michael, D. M. D. Understanding degradation mechanisms and improving stability of perovskite photovoltaics. *Chem. Rev.* **2019**, *119*, 3418−3451.

(15) Sutton, R. J.; Eperon, G. E.; Miranda, L.; Parrott, E. S.; Kamino, B. A.; Patel, J. B.; Hörantner, M. T.; Johnston, M. B.; Haghighirad, A. A.; Moore, D. T.; Snaith, H. J. Bandgap-tunable cesium lead halide perovskites with high thermal stability for efficient solar cells. *Adv. Energy Mater.* **2016**, *6*, No. 1502458.

(16) Leguy, A. M. A.; Hu, Y.; Campoy-quiles, M.; Alonso, M. I.; Weber, O. J.; Azarhoosh, P.; Van schilfgaarde, M.; Weller, M. T.; Bein, T.; Nelson, J.; Docampo, P.; Barnes, P. R. F. Reversible hydration of $CH_3NH_3PbI_3$ in films, single crystals, and solar cells. *Chem. Mater.* **2015**, *27*, 3397−3407.

(17) Jiang, Q.; Zhao, Y.; Zhang, X.; Yang, X.; Chen, Y.; Chu, Z.; Ye, Q.; Li, X.; Yin, Z.; You, J. Surface passivation of perovskite film for efficient solar cells. *Nat. Photonics* **2019**, *13*, 460−466.

(18) Zhang, X.; Baral, P.; Chakraborty, N.; Garden, K.; Shen, L.; Vijayaraghavan, S. N.; Cao, Z.; Yan, F.; Gong, X.; Whittaker-brooks, L.; Wang, H. Blade coating inverted perovskite solar cells with vacuum-assisted nucleation based on bottom quasi-2D passivation. *Sol. RRL* **2023**, *7*, No. 2200900.

(19) Zheng, L.; Shen, L.; Zhu, T.; Zhang, D.; Zheng, J.; Gong, X. Stable and efficient perovskite solar cells by discrete two-dimensional perovskites capped on the three-dimensional perovskites bilayer thin film. *Nano Energy* **2022**, *96*, No. 107126.

(20) Leung, T. L.; Ahmad, I.; Syed, A. A.; Ng, A. M. C.; Popović, J.; Djurišić, A. B. Stability of 2D and quasi-2D perovskite materials and devices. *Commun. Mater.* **2022**, *3*, 63.

(21) Wang, K.; Wu, C.; Yang, D.; Jiang, Y.; Priya, S. Quasi-two-dimensional halide perovskite single crystal photodetector. *ACS Nano* **2018**, *12*, 4919−4929.

(22) Zhu, T.; Shen, L.; Xun, S.; Sarmiento, J. S.; Yang, Y.; Zheng, L.; Li, H.; Wang, H.; Bredas, J.-L.; Gong, X. High-performance ternary perovskite−organic solar cells. *Adv. Mater.* **2022**, *34*, No. 2109348.

(23) Zhou, T.; Lai, H.; Liu, T.; Lu, D.; Wan, X.; Zhang, X.; Liu, Y.; Chen, Y. Highly efficient and stable solar cells based on crystalline oriented 2D/3D hybrid perovskite. *Adv. Mater.* **2019**, *31*, No. 1901242.

(24) Mao, L.; Stoumpos, C. C.; Kanatzidis, M. G. Two-dimensional hybrid halide perovskites: principles and promises. *J. Am. Chem. Soc.* **2019**, *141*, 1171−1190.

(25) Mao, L.; Ke, W.; Pedesseau, L.; Wu, Y.; Katan, C.; Even, J.; Wasielewski, M. R.; Stoumpos, C. C.; Kanatzidis, M. G. Hybrid Dion−Jacobson 2D lead iodide perovskites. *J. Am. Chem. Soc.* **2018**, *140*, 3775−3783.

(26) Zhou, N.; Huang, B.; Sun, M.; Zhang, Y.; Li, L.; Lun, Y.; Wang, X.; Hong, J.; Chen, Q.; Zhou, H. The spacer cations interplay for efficient and stable layered 2D perovskite solar cells. *Adv. Energy Mater.* **2020**, *10*, No. 1901566.

(27) Zhang, Y.; Chen, J.; Lian, X.; Qin, M.; Li, J.; Andersen, T. R.; Lu, X.; Wu, G.; Li, H.; Chen, H. Highly efficient guanidinium-based quasi 2D perovskite solar cells via a two-step post-treatment process. *Small Methods* **2019**, *3*, No. 1900375.
(28) Cao, D. H.; Stoumpos, C. C.; Farha, O. K.; Hupp, J. T.; Kanatzidis, M. G. 2D homologous perovskites as light-absorbing materials for solar cell applications. *J. Am. Chem. Soc.* **2015**, *137*, 7843−7850.
(29) Qiu, J.; Xia, Y.; Zheng, Y.; Hui, W.; Gu, H.; Yuan, W.; Yu, H.; Chao, L.; Niu, T.; Yang, Y.; Gao, X.; Chen, Y.; Huang, W. 2D intermediate suppression for efficient ruddlesden−popper (RP) phase lead-free perovskite solar cells. *ACS Energy Lett.* **2019**, *4*, 1513−1520.
(30) Zhang, F.; Kim, D. H.; Lu, H.; Park, J.-S.; Larson, B. W.; Hu, J.; Gao, L.; Xiao, C.; Reid, O. G.; Chen, X.; Zhao, Q.; Ndione, P. F.; Berry, J. J.; You, W.; Walsh, A.; Beard, M. C.; Zhu, K. Enhanced charge transport in 2D perovskites via fluorination of organic cation. *J. Am. Chem. Soc.* **2019**, *141*, 5972−5979.
(31) Zhu, T.; Gong, X. low-dimensional perovskite materials and their optoelectronics. *Info Mat* **2021**, *3*, 1039−1069.
(32) Liu, Y.; Ye, H.; Zhang, Y.; Zhao, K.; Yang, Z.; Yuan, Y.; Wu, H.; Zhao, G.; Yang, Z.; Tang, J.; Xu, Z.; Liu, S. F. Surface-tension-controlled crystallization for high-quality 2D perovskite single crystals for ultrahigh photodetection. *Matter.* **2019**, *1*, 465−480.
(33) Wang, J.; Li, J.; Lan, S.; Fang, C.; Shen, H.; Xiong, Q.; Li, D. Controllable growth of centimeter-sized 2D perovskite heterostructures for highly narrow dual-band photodetectors. *ACS Nano* **2019**, *13*, 5473−5484.
(34) Dong, R.; Lan, C.; Li, F.; Yip, S.; Ho, J. C. Incorporating mixed cations in quasi-2D perovskites for high-performance and flexible photodetectors. *Nanoscale Horiz.* **2019**, *4*, 1342−1352.
(35) Zhu, T.; Shen, L.; Chen, H.; Yang, Y.; Zheng, L.; Chen, R.; Zheng, J.; Wang, J.; Gong, X. Conjugated molecule based 2D perovskites for high-performance perovskite solar cells. *J. Mater. Chem. A* **2021**, *9*, 21910−21917.
(36) Xue, J. J.; Wang, R.; Chen, X. H.; Wang, L.; Yao, C. L.; Jin, X. Y.; Wang, K. L.; Huang, W. H.; Huang, T. Y.; Zhao, Y. P.; Yang, Y. Reconfiguring the band-edge states of photovoltaic perovskites by conjugated organic cations. *Science* **2021**, *371*, 636−640.
(37) Rodríguez-romero, J.; Hames, B. C.; Mora-seró, I.; Barea, E. M. Conjugated organic cations to improve the optoelectronic properties of 2D/3D perovskites. *ACS Energy Lett.* **2017**, *2*, 1969−1970.
(38) Yang, J.; He, T. W.; Li, M.; Li, G. X.; Liu, H. R.; Xu, J. J.; Zhang, M.; Zuo, W. W.; Qin, R. P.; Aldamasy, M. H.; Yuan, M. J.; Li, Z.; Byranvand, M. M.; Saliba, M.; Abate, A. π-conjugated carbazole cations enable wet-stable quasi-2D perovskite photovoltaics. *ACS Energy Lett.* **2022**, *7*, 4451−4458.
(39) Ran, C. X.; Gao, W. Y.; Li, J. R.; Xi, J.; Li, L.; Dai, J. F.; Yang, Y. G.; Gao, X. Y.; Dong, H.; Jiao, B.; Spanopoulos, I.; Malliakas, C. D.; Hou, X.; Kanatzidis, M. G.; Wu, Z. X. Conjugated organic cations enable efficient self-healing $FASnI_3$ solar cells. *Joule* **2019**, *3*, 3072−3087.
(40) Gao, Y.; Dou, L. T. Organic semiconductor-incorporated two-dimensional halide perovskites. *Natl. Sci. Rev.* **2022**, *9*, No. nwab111.
(41) Shi, J. S.; Jin, X.; Wu, Y. Z.; Shao, M. Mixed bulky cations for efficient and stable ruddlesden−popper perovskite solar cells. *APL Mater.* **2020**, *8*, 101102.
(42) Ye, J. Y.; Tong, J.; Hu, J.; Xiao, C.; Lu, H.; Dunfield, S. P.; Kim, D. H.; Chen, X.; Larson, B. W.; Hao, J. Enhancing charge transport of 2D perovskite passivation agent for wide-bandgap perovskite solar cells beyond 21%. *Sol. RRL* **2020**, *4*, No. 2000082.
(43) Shen, L.; Wu, H.; Zhu, T.; Zhang, X.; Sawwan, H.; Wang, H.; Gong, X. Three- and two-dimensional mixed metal halide perovskites for high-performance photovoltaics. *Org. Electron.* **2023**, *118*, No. 106796.
(44) Bube, R. H. Trap density determination by space-charge-limited currents. *J. Appl. Phys.* **1962**, *33*, 1733−1737.
(45) Le corre, V. M.; Duijnstee, E. A.; El tambouli, O.; Ball, J. M.; Snaith, H. J.; Lim, J.; Koster, L. J. A. Revealing charge carrier mobility and defect densities in metal halide perovskites via space-charge-limited current measurements. *ACS Energy Lett.* **2021**, *6*, 1087−1094.
(46) Yang, Y.; Yan, Y.; Yang, M.; Choi, S.; Zhu, K.; Luther, J. M.; Beard, M. C. Low surface recombination velocity in solution-grown $CH_3NH_3PbBr_3$ perovskite single crystal. *Nat. Commun.* **2015**, *6*, 7961.
(47) Byranvand, M. M.; Kim, T.; Song, S.; Kang, G.; Ryu, S. U.; Park, T. p-type CuI islands on TiO_2 electron transport layer for a highly efficient planar-perovskite solar cell with negligible hysteresis. *Adv. Energy Mater.* **2018**, *8*, No. 1702235.
(48) Wang, Z. P.; Lin, Q. Q.; Chmiel, F. P.; Sakai, N.; Herz, L. M.; Snaith, H. J. Efficient ambient-air-stable solar cells with 2D−3D heterostructured butylammonium-caesium-formamidinium lead halide perovskites. *Nat. Energy* **2017**, *2*, No. 17135.
(49) Zhao, D.; Gao, D. P.; Wu, X.; Li, B.; Zhang, S. F.; Li, Z.; Wang, Q.; Wu, Z. X.; Zhang, C. L.; Choy, W. C. H.; Zhong, X. Y.; He, Q. Y.; Zhu, Z. L. Efficient and stable 3D/2D perovskite solar cells through vertical heterostructures with $(BA)_4AgBiBr_8$ nanosheets. *Adv. Mater.* **2022**, *34*, No. 2204661.
(50) Baral, P.; Zhang, X.; Garden, K.; Chakraborty, N.; Shen, L.; Cao, Z.; Gong, X.; Whittaker-brooks, L.; Wang, H. Efficient and stable perovskite solar cells based on blade-coated $CH_3NH_3PbI_3$ Thin films fabricated using "green" solvents under ambient conditions. *Org. Electron.* **2023**, *116*, No. 106763.
(51) Zhou, M.; Sarmiento, J. S.; Fei, C.; Wang, H. Charge transfer and diffusion at the perovskite/PCBM interface probed by transient absorption and reflection. *J. Phys. Chem. C* **2019**, *123*, 22095−22103.
(52) Wang, Z.; Lin, Q.; Chmiel, F. P.; Sakai, N.; Herz, L. M.; Snaith, H. J. Efficient ambient-air-stable solar cells with 2D−3D heterostructured butylammonium-caesium-formamidinium lead halide perovskites. *Nat. Energy* **2017**, *2*, No. 17135.
(53) Laban, W. A.; Etgar, L. Depleted hole conductor-free lead halide iodide heterojunction solar cells. *Energy Environ. Sci.* **2013**, *6*, 3249.
(54) Chen, Y.; Sun, Y.; Peng, J. J.; Tang, J. H.; Zheng, K. B.; Liang, Z. Q. 2D ruddlesden−popper perovskites for optoelectronics. *Adv. Mater.* **2017**, *30*, No. 1703487.
(55) Zhao, Q.; Wu, R.; Zhang, Z.; et al. Achieving efficient inverted planar perovskite solar cells with nondoped PTAA as a hole transport layer. *Org. Electron.* **2019**, *71*, 106−112.
(56) Wang, N.; Yu, J.; Zang, Y.; Huang, J.; Jiang, Y. Effect of buffer layers on the performance of organic photovoltaic cells based on copper phthalocyanine and C60. *Sol. Energy Mater. Sol. Cells* **2010**, *94*, 263−266.
(57) Yu, Y.; Xia, J.; Liang, Y. Basic understanding of perovskite solar cells and passivation mechanism. *AIP Adv.* **2022**, *12*, No. 055307.
(58) Jafari, F.; Patil, B. R.; Mohtaram, F.; et al. Inverted organic solar cells with non-clustering bathocuproine (BCP) cathode interlayers obtained by fullerene doping. *Sci. Rep.* **2019**, *9*, 10422.
(59) Zou, Y.; Eichhorn, J.; Rieger, S.; Zheng, Y.; Yuan, S.; Wolz, L.; Spanier, L. V.; Heger, J. E.; Yin, S.; Everett, C. R.; Dai, L.; Schewartzkopf, M.; Mu, C.; Roth, S. V.; Sharp, I. D.; Chen, C.-C.; Feldmann, J.; Stranks, S. D.; Müller-buschbaum, P. Ionic liquids tailoring crystal orientation and electronic properties for stable perovskite solar cells. *Nano Energy* **2023**, *112*, No. 108449.
(60) Seifter, J.; Sun, Y.; Heeger, A. J. Transient photocurrent response of small-molecule bulk heterojunction solar cells. *Adv. Mater.* **2014**, *26*, 2486−2493.
(61) Wang, K.; Zheng, L.; Zhu, T.; Liu, L.; Becker, M. L.; Gong, X. High performance perovskites solar cells by hybrid perovskites co-crystallized with poly(ethylene oxide). *Nano Energy* **2020**, *67*, No. 104229.
(62) Sze, S. M.; Ng, K. K. *Physics of Semiconductor Devices*, 1st ed.; Wiley, 2006.
(63) Gong, X.; Tong, M.; Xia, Y.; Cai, W.; Moon, J. S.; Cao, Y.; Yu, G.; Shieh, C.-L.; Nilsson, B.; Heeger, A. J. High-detectivity polymer photodetectors with spectral response from 300 to 1450 nm. *Science* **2009**, *325*, 1665−1667.

https://doi.org/10.1021/acsami.4c00288
ACS Appl. Mater. Interfaces 2024, 16, 19318−19329

(64) Zheng, L.; Zhu, T.; Xu, W.; Zheng, J.; Liu, L.; Gong, X. Ultrasensitive perovskite photodetectors by co partially substituted hybrid perovskite. *ACS Sustain. Chem. Eng.* **2018**, *6*, 12055−12060.
(65) Chen, R.; Shen, L.; Zheng, L.; Zhu, T.; Liu, Y.; Liu, L.; Zheng, J.; Gong, X. Two-/three-dimensional perovskite bilayer thin films post-treated with solvent vapor for high-performance perovskite photovoltaics. *ACS Appl. Mater. Interfaces* **2021**, *13*, 49104−49113.
(66) Jha, A. R.; Jha, A. R.; Jha, D. A. *Infrared technology: applications to electro-optics, photonic devices, and sensors*; Wiley: New York, 2000.
(67) Hegedus, S. S.; Shafarman, W. N. Thin-film solar cells: device measurements and analysis. *Prog. Photovolt.: Res. Appl.* **2004**, *12*, 155−176.
(68) Shen, L.; Zhu, T.; Zhang, X.; Gong, K.; Wang, H.; Gong, X. Bulk heterojunction perovskite solar cells incorporated with p-type low optical gap conjugated polymers. *Nano Energy* **2022**, *93*, No. 106907.

https://doi.org/10.1021/acsami.4c00288
ACS Appl. Mater. Interfaces 2024, 16, 19318−19329